Core Excitations of Uranyl in Cs2UO2Cl4 from Relativistic Embedded Damped Response Time-Dependent Density Functional Theory Calculations

Wilken Aldair Misael, André Severo Pereira Gomes

To cite this version:

Wilken Aldair Misael, André Severo Pereira Gomes. Core Excitations of Uranyl in Cs2UO2Cl4 from Relativistic Embedded Damped Response Time-Dependent Density Functional Theory Calculations. Inorganic Chemistry, 2023, 62, pp.11589-11601. 10.1021/acs.inorgchem.3c01302 . hal-03990050

HAL Id: hal-03990050
https://hal.science/hal-03990050v1

Submitted on 15 Jul 2024

Inorganic Chemistry

pubs.acs.org/IC

Article

Core Excitations of Uranyl in $Cs_2UO_2Cl_4$ from Relativistic Embedded Damped Response Time-Dependent Density Functional Theory Calculations

Wilken Aldair Misael and André Severo Pereira Gomes*

Cite This: *Inorg. Chem.* 2023, 62, 11589−11601

Read Online

ACCESS | Metrics & More | Article Recommendations | Supporting Information

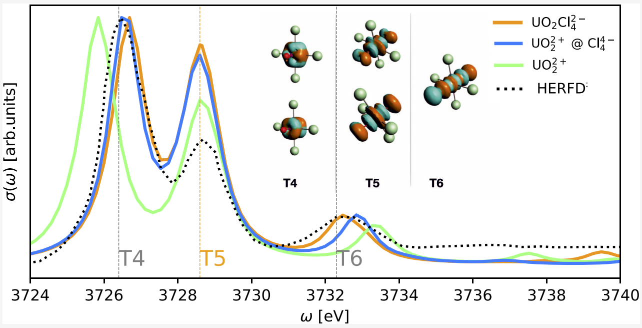

ABSTRACT: X-ray spectroscopies, by their high selectivity and sensitivity to the chemical environment around the atoms probed, provide significant insights into the electronic structures of molecules and materials. Interpreting experimental results requires reliable theoretical models, accounting for environmental, relativistic, electron correlation, and orbital relaxation effects in a balanced manner. In this work, we present a protocol for the simulation of core excited spectra with damped response time-dependent density functional theory based on the Dirac−Coulomb Hamiltonian (4c-DR-TD-DFT), in which environmental effects are accounted for through the frozen density embedding (FDE) method. We showcase this approach for the uranium M_4- and L_3-edges and oxygen K-edge of the uranyl tetrachloride ($UO_2Cl_4^{2-}$) unit as found in a host $Cs_2UO_2Cl_4$ crystal. We have found that the 4c-DR-TD-DFT simulations yield excitation spectra that very closely match the experiment for the uranium M_4-edge and the oxygen K-edge, with good agreement for the broad experimental spectra for the L_3-edge. By decomposing the complex polarizability in terms of its components, we have been able to correlate our results with angle-resolved spectra. We have observed that for all edges, but in particular the uranium M_4-edge, an embedded model in which the chloride ligands are replaced by an embedding potential reproduces rather well the spectral profile obtained for $UO_2Cl_4^{2-}$. Our results underscore the importance of the equatorial ligands to simulating core spectra at both uranium and oxygen edges.

■ INTRODUCTION

Actinides are relevant to modern societies, first and foremost due to their central role in the nuclear industry[1−5] and the potentially harmful effects that can occur with their release in the biosphere in the case of industrial accidents.[6−9] In more recent years, the peculiar properties of materials containing actinides have also spurred interest from a fundamental perspective as well as for industrial applications in catalysis,[10−12] materials,[11,13−16] and nanotechnology.[17−20]

As these properties stem from subtle differences in the electronic structures of different compounds,[21−24] a key objective in actinide science is to characterize their electronic structures under different conditions. To this end, spectroscopies involving core electrons[25−29] are particularly interesting, since they are very sensitive to changes in the oxidation state and the local chemical environment of actinides.[30−34]

In recent years, with the development of high-energy fourth-generation synchrotron radiation facilities around the world and the availability of X-ray free electron lasers (XFELs),[27,29,35] one has witnessed the development and applications of high-energy resolution X-ray spectroscopy (HERXS) to actinides.[36−41]

The set of HERXS techniques includes spectroscopies such as high-energy resolution fluorescence detected X-ray absorption near edge structure (HERFD-XANES), high-energy-resolution Auger detection (HERAD-XANES), high-energy X-ray scattering (HEXS), and extended X-ray absorption fine structure (EXAFS).[10,33,38,41−43] For actinides, a particularly appealing feature of HERXS measurements is their larger penetration depth, which allows for smaller samples,[28,36−39,44] minimizing the need for extensive radiation exposure protection measures. These experiments also offer increased sensitivity in probing processes that involve transitions to and from d and f orbitals, with the latter playing a pivotal role in actinide bonding.[45−50]

These experimental developments, and the inherent complexities of interpreting the data generated, have stimulated the use of accurate molecular electronic structure

Received: April 21, 2023
Published: July 11, 2023

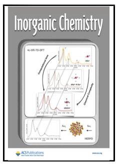

https://doi.org/10.1021/acs.inorgchem.3c01302
Inorg. Chem. 2023, 62, 11589−11601

methods as a means to interpret, predict, and suggest new measurements in the X-ray range.[51−56]

While it has long been established that in this regime, theoretical approaches must properly account for electron correlation[53,54,57−60] and orbital relaxation[56,61−64] in order to yield reliable results, the importance of relativistic effects,[65−69] indispensable for heavy elements, is now also recognized for elements as light as those in the second row of the periodic table.

Since most measurements of core spectra are done for molecules in the gas phase, it may become necessary to include environmental effects in the calculations. This can be done efficiently and accurately with embedding approaches,[70−73] whereby a sufficiently accurate fully quantum mechanical (QM) description is applied to the region of interest, and a significant portion of the system is represented via quantum (QM/QM) or classically derived (QM/MM) effective operators, without any a priori assumptions on the nature of the region of interest or the environment, which makes them potentially more flexible than other proven approaches based on, e.g., explicit and continuum (implicit) solvation models[74−77] and ligand-field theory.[78−80]

Among actinides, a particularly important class of complexes contains the uranyl (UO_2^{n+}, $n = 1, 2$) moiety, which is ubiquitous in the solution and solid-state chemistry of uranium. It is known to show very strong U−O triple bonds[21] and generally presents a linear O−U−O geometry, with other ligands coordinating with uranium in the equatorial plane, via less strong interactions. The core spectroscopy of uranyl coordination complexes has been investigated with several theoretical methods, such as complete and restricted active space self-consistent field,[50,81−85] crystal ligand-field multiplet theory and its variations,[34,43,80,86−89] density functional theory in its different flavors,[43,47,57,90−93] self-consistent real-space multiple scattering,[42,43] static exchange approximation,[57] and perturbation theory.[57]

For molecular-based approaches, relativistic correlated many-body approaches[83−85,94] are among the most accurate approaches that can be used, but their relatively high computational cost makes them difficult to employ for experimentally relevant systems in the condensed phase. In the case of absorption spectroscopy, it has been found that with a suitable choice of density functional approximation (DFA)—notably the CAM-B3LYP functional[95]—density functional theory (DFT) can provide reliable excitation energies of actinides in the ultraviolet−visible region,[76,77,96−99] with a recent, very comprehensive work by Konecny et al.[93] employing the four-component damped response time-dependent density functional theory (4c-DR-TD-DFT) formalism, indicating that the same holds for the core excited states of uranium complexes.

One aspect that, in our view, was not sufficiently addressed in the work by Konecny and co-workers, is the extent to which the environment can play a role in the spectral features. While Konecny et al.[93] provided a comparison between theory and the experiment for the uranium M_4-edge of uranium nitrate oxide ($UO_2(NO_3)_2$), there are other systems such as the $Cs_2UO_2Cl_4$ crystal, for which there are HERFD-XANES spectra for the uranium M_4-edge as well as XANES spectra for the uranium L_3-edge[47] and the oxygen K-edge,[100] which could provide more comprehensive comparisons to the experiment.

The present work, therefore, aims to employ embedding approaches and the 4c-DR-TD-DFT formalism to investigate the effect of the chloride ligands bound to the equatorial plane of uranyl in the $Cs_2UO_2Cl_4$ crystal on the oxygen K-edge and uranium M_4- and L_3-edge excited states, with a detailed comparison to experimental results available in the literature for this system.

The structure of this article is as follows. We start by presenting the computational details from our calculations, followed by our results for the simulated X-ray absorption spectra. Finally, we present our conclusions and some future perspectives.

■ COMPUTATIONAL DETAILS

DR-TD-DFT and the corresponding 4c-DR-TD-DFT-in-DFT calculations were performed in the DIRAC22[101] version of the `DIRAC` electronic structure code,[102] as well as development snapshots (`34fbd49`, `4b35e48`, `d70bbe283`, `e061718`, `e0617189f6`, `e7e2094`). We employed Dyall's all-electron basis sets of double- and triple-ζ quality[103,104] for uranium and Dunning's cc-pVTZ basis set[105] for all other atoms. These basis sets were left uncontracted. We employed a Gaussian nuclear model in all calculations.[106]

For all DFT calculations with `DIRAC`, we employed the Dirac−Coulomb (^{4}DC) Hamiltonian and the long-range corrected CAM-B3LYP[95] functional.

In all of our calculations, the structures employed were based on the experimental crystal structure of $Cs_2UO_2Cl_4$ reported by Watkin et al.,[107] whose U−O and U−Cl bond lengths are 1.774 and 2.673 Å, respectively. For the embedding calculations, we employed the same structural models and subsystem partitioning as outlined by Gomes et al.[97] All calculations on bare uranyl and uranyl tetrachloride were carried out in $D_{\infty h}$ and D_{2h} symmetries, respectively, while for embedded uranyl simulations, the crystalline site symmetry (C_{2h}) was used.

The embedding potentials employed here were obtained from freeze−thaw calculations employing the scalar relativistic ZORA Hamiltonian,[108] TZ2P basis sets, the PW91k kinetic energy functional[109] and the PBE exchange−correlation functional[110] for the nonadditive terms, and subsystem energies. These calculations were carried out via the `PyADF` scripting framework[111] and the embedding potentials were subsequently imported into the `DIRAC` calculations.

For the 4c-DR-TD-DFT calculations, we selected a frequency range that covered the energy ranges bracketing the main features in the oxygen K-edge (around 510−540 eV) and the uranium M_4- and L_3-edges (around 3680−3710 and 17 070−17 100 eV, respectively). Given the expected shift in these simulations, the first frequency for each interval was obtained through TD-DFT simulations using the restricted-energy window scheme (REW-TD-DFT)[112] implementation on `DIRAC`.

In addition to the calculations with `DIRAC`, for the uranyl tetrachloride dianion species, we carried out standard (without embedding) TD-DFT calculations with the X2C Hamiltonian (including spin−orbit coupling, 2c-TD-DFT), triple-ζ basis functions with two polarization functions (TZ2P),[113] and the CAM-B3LYP functional with the Amsterdam Density Functional (ADF) software package.[114] As 4c-DR-TD-DFT calculations including spin−orbit coupling are not currently

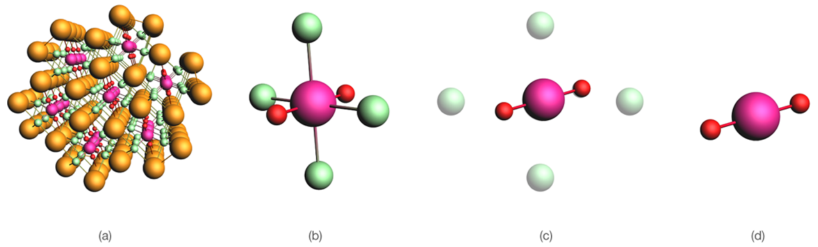

Figure 1. Reference system for this study: (a) dicesium uranyl(VI) tetrachloride crystal ($Cs_2UO_2Cl_4$). Models here investigated: (b) uranyl(VI) tetrachloride dianion, $UO_2Cl_4^{2-}$, (c) uranyl(VI) ion in the FDE embedding potential of four chloride atoms, UO_2^{2+}@Cl_4^{4-}, and (d) bare uranyl(VI) ion, UO_2^{2+} (cesium: orange; uranium: pink; oxygen: red; chlorine: green). See Gomes et al.[97] for further details on the structural models.

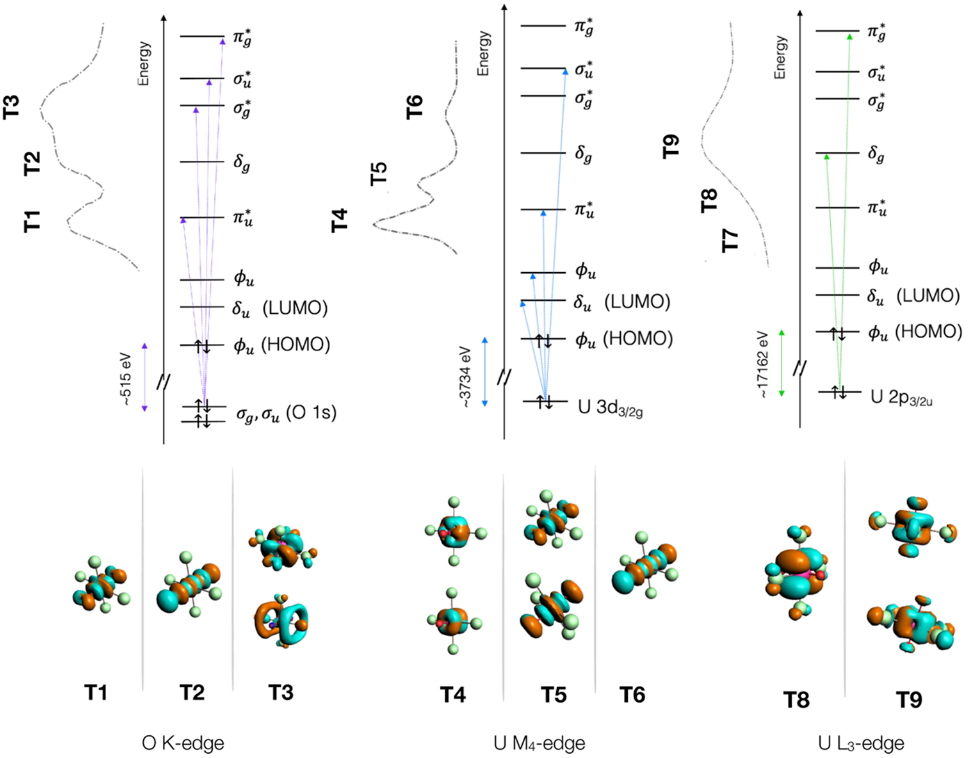

Figure 2. Top: qualitative MO diagram for the relevant orbitals of uranyl being accessed in this work. Bottom: dominant 2c-TD natural transition orbitals (NTOs) for the peaks pertaining to the oxygen K-edge and uranium M_4- and L_3-edges. Plots have employed 0.03 as the isosurface value. See the text for the nature of the transitions (labeled **T1**−**T9**). We do not display NTOs for **T7**, as the associated transition does not have intensity within the dipole approximation and is therefore not discussed.

supported by ADF, we employed 2c-REW-TD-DFT calculations to target the core excited states of interest and employed the Tamm−Dancoff approximation (TDA),[115] as it yielded spectra of the same quality as standard TD-DFT calculations at a lower computational cost. A comparison of TD-DFT and TDA can be found in Figures S1 and S2 in the Supporting Information.

Due to a lack of equivalent functionality in `DIRAC`, from the ADF 2c-REW-TD-DFT calculations, we obtained natural transition orbitals (NTOs),[116] which we used to provide a qualitative analysis of the changes to the electronic structure involved in the core excitations of uranyl tetrachloride.

For simplicity, in the following, we shall refer to our 4c-DR-TD-CAM-B3LYP calculations as 4c-DR and to our 2c-REW-TD-DFT and 2c-REW-TD-DFT-TDA CAM-B3LYP calculations as 2c-TD and 2c-TDA, respectively.

■ RESULTS AND DISCUSSION

In the following section, we present the theoretical absorption spectra at the oxygen K-edge and uranium M_4- and L_3-edges of the uranyl tetrachloride dianion ($UO_2Cl_4^{2-}$), a model in which the chloride ions bound to the equatorial plane of the uranyl ion (UO_2^{2+}) are represented by an frozen density embedding (FDE) embedding potential (UO_2^{2+}@Cl_4^{4-}) and the uranyl ion without any chloride ligands (structures **b**, **c**, and **d**, respectively, in Figure 1).

Before discussing the relative performance of these different models, we focus on a comparison between our results for $UO_2Cl_4^{2-}$ and the available experimental spectra recorded for the $Cs_2UO_2Cl_4$ crystal. Our results will be interpreted on the basis of the dominant NTOs for each peak, depicted in Figure 2, whereas the simulated spectra are depicted in Figure 3.

Features in the X-ray Absorption Spectra. The absorption spectrum of the $Cs_2UO_2Cl_4$ crystal has been utilized in multiple studies as a tool to examine the electric

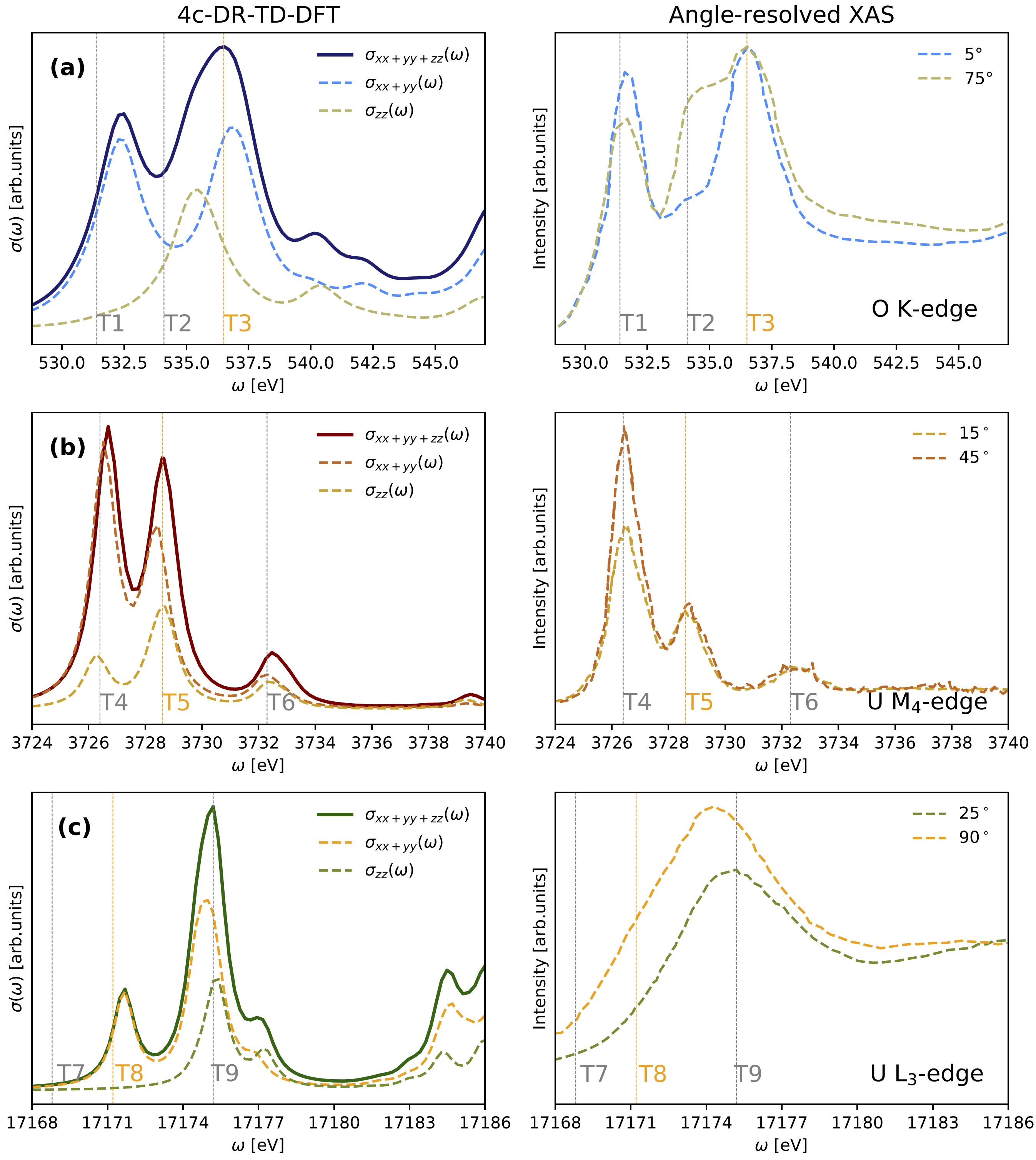

Figure 3. Left: partial (dashed) and total (solid) contributions to total oscillator strengths in the 4c-DR XAS spectra at (a) oxygen K-edge and uranium (b) M_4- and (c) U L_3-edges of $UO_2Cl_4^{2-}$. Right: experimental data ($Cs_2UO_2Cl_4$) at the O K-edge (digitized with permission from Denning et al.[100] Copyright 2002 AIP Publishing) and U M_4- and L_3-edges (digitized from Vitova et al.[47] Copyright 2015 American Chemical Society). The angle indicated in the figures corresponds to the angle between the incident light beam and the O−U−O axis.

properties of the uranyl(VI) ion in diverse environments, including one- and two-photon absorption at visible light.[105,117] The X-ray absorption near edge structure (XANES) spectrum at the oxygen K-edge of $Cs_2UO_2Cl_4$ was first reported by Denning et al.[100] in the early 2000s, and the high-energy-resolution fluorescence detection (HERFD) spectra at the uranium M_4- and L_3-edges of $Cs_2UO_2Cl_4$ were reported by Vitova et al.[47] in the past decade.

As previously reported by Denning et al.,[100] the O K-edge absorption spectrum (Figure 3a) exhibits three prominent features identified as (**T1**) a low-intensity pre-edge feature at 531.4 eV corresponding to an O 1s → π_u^* transition, followed by (**T2**) an intermediate-intensity pre-edge feature at around 534.1 eV, arising from an O 1s → σ_u^* transition, and (**T3**) the white-line feature at 536.5 eV, where an O 1s → π_g^* transition is observed.

Using the HERFD mode for the evaluation of the U M_4-edge spectra, it is possible to achieve experimental spectral widths below the natural core-hole lifetime broadening of approximately 4 eV. As a result, the high-resolution U M_4-edge spectra in $Cs_2UO_2Cl_4$ exhibit three well-defined features (Figure 3b), which were reported in previous studies:[33,47] (**T4**) U $3d_{5/2g} \rightarrow 5f\delta_u$ and U $3d_{5/2g} \rightarrow 5f\phi_u$ excitation observed at 3726.4 eV, (**T5**) U $3d_{5/2g} \rightarrow 5f\pi_u^*$ resonance at 3728.6 eV, and a satellite peak (**T6**) U $3d_{5/2g} \rightarrow 5f\sigma_u^*$ at 3732.3 eV.

Interpreting the spectra at the U L_3-edge (Figure 3c) remains challenging due to the significant core-hole lifetime width spanned in this absorption edge, which extends between 7.4 and 8.4 eV.[118,119] This results in a significant portion of the spectral content being obscured.

The first transition in this spectra is a $2p_{3/2u} \rightarrow 5f$ quadrupolar transition (**T7**) at 17168.8 eV, which is absent in our simulations. This is due to our use of the dipole approximation, so that by symmetry, the associated transition does not carry any intensity. Beyond that, the experimental white line is observed at 17 175.2 eV, and our simulations predict that this feature is mainly composed of (**T8**, **T9**) two $2p_{3/2u} \rightarrow (6d\delta_g, 6d\pi_g)$ contributions, with a separation of 3.5 eV.

From the NTO analysis, we see that the dominant contributions involve low-lying virtual orbitals centered around the uranyl moiety, and as discussed below, the associated excited states will be rather well described. That said, one should be careful if highly diffuse orbitals such as Rydberg orbitals[120,121] are found to be involved in the transitions, since apart from the general difficulty of describing such orbitals with standard Gaussian basis sets,[122] not all density functional approximations can describe long-range interactions as accurately as CAM-B3LYP.[96]

Theoretical versus Experimental Peak Positions. All of our calculated transition energies shown in Table 1 were considered for the analysis. We observe that these are shifted in a very systematic manner to higher energies with respect to the experiment, with these differences of energy becoming increasingly pronounced at higher absorption edges. For instance, at the O K-edge, the energy shift values for the 2c-TDA and 4c-DR simulations are, respectively, 13.3 and 13.8 eV, whereas for the U L_3-edge, these values are 95.2 and 86.3 eV. Therefore, in order to compare the theoretical and experimental results, we have aligned these based on specific transitions, identified by orange vertical lines in Figure 3.

The increasing discrepancy between experimental and theoretical peak positions (and hence the increase in the value of the shift to be applied to theoretical results) for deeper cores is related to the difficulty of TD-DFT to properly account for the orbital relaxation that should accompany the creation of a core hole, which will be increasingly important, as the core orbitals under consideration become closer to the nucleus.

The magnitude of orbital relaxation effects for the deeper core in heavy elements is clearly illustrated for ionization energies, obtained for small actinide species[57] with state-specific correlated methods (ΔMP2) or for heavy halogenated species[94,123,124] employing the equation of motion coupled-cluster approaches (CVS-EOM-IP-CCSD), with the results by Halbert et al.[94] and Knecht et al.,[124] illustrating that (small) differences between two- and four-component Hamiltonians as seen here may arise, depending on which a two-component approach is used. More recently, orbital relaxation has also been investigated for excitation energies at the U M_4-edge of bare uranyl using multiconfigurational approaches.[81,83,84]

Table 1. Transition Energies (in eV) Calculated Using 2c-TDA and 4c-DR Compared to Experimental Values for the O K-Edge, U M_4-Edge, and U L_3-Edge[a]

	O K-edge		
	T1	**T2**	**T3**
	O 1s → π_u^*	O 1s → σ_u^*	O 1s → π_g^*
2c-TDA	518.6 (−12.8)	521.4 (−12.7)	523.2 (−13.3)
4c-DR	518.5 (−12.9)	521.4 (−12.7)	522.7 (−13.8)
exp.[100]	531.4	534.1	536.5
	U M_4-edge		
	T4	**T5**	**T6**
	U $3d_{5/2g} \rightarrow 5f\delta_u$	U $3d_{5/2g} \rightarrow \pi_u^*$	U $3d_{5/2g} \rightarrow 5f\sigma_u^*$
2c-TDA	3686.6 (−40.8)	3688.4 (−40.2)	3692.5 (−39.8)
4c-DR	3689.5 (−36.9)	3691.4 (−37.2)	3695.3 (−37.0)
exp.[47]	3726.4	3728.6	3732.3
	U L_3-edge		
	T7	**T8**	**T9**
	U $2p_{3/2u} \rightarrow 5f$	U $2p_{3/2u} \rightarrow 6d\delta_g$	U $2p_{3/2u} \rightarrow 6d\pi_g$
2c-TDA		17 076.5 (−95.2)	17 080.0 (−95.2)
4c-DR		17 085.4 (−86.3)	17 088.9 (−86.3)
exp.[47]	17 168.8	17 171.7	17 175.2

[a] Shifts with respect to the experiment (in eV) are shown in parenthesis.

In the latter case, Polly et al.[83] evaluated the performance of various active spaces in SO-RASSCF and SO-RASPT2 simulations. Their results to excitation energies at the U M_4-edge were found to overestimate experimental values by 12.9 and 17.4 eV at RASSCF and RASPT2 theory levels, respectively. This corresponds to about half of the over-estimation found for our 4c-DR and 2c-TDA results (37.2 and 39.8 eV, respectively).

The relatively modest changes upon including dynamical electron correlation (about 5 eV) are consistent with the findings of South et al.[57] on the contribution from electron correlation (at the MP2 level) to the binding energies in uranyl, as most of the core-hole relaxation is coming from the orbital optimization enabled by the RASSCF approach. It is nevertheless interesting to note that the RASSCF calculations are closer to the experiment than RASPT2, suggesting a possible cancellation of errors when comparing bare uranyl to the experimental system. We will return to this point when discussing the performance of embedding.

As final remarks, we note that the damping factors employed for determining the 4c-DR absorption spectra shown in Figure 3 are not arbitrary but selected to best reflect the profile observed in the experimental data for the $Cs_2UO_2Cl_4$ crystal, after exploring different values for each edge. For the oxygen K-edge, the value is somewhat larger ($\gamma = 1.0$ eV) than that for the uranium M_4- and L_3-edges ($\gamma = 0.5$ eV), but, nevertheless, our results show that with these choices, the key features of both conventional and high-resolution spectra can be clearly identified.

Furthermore, the broadening profile presented in Figure 3 was chosen to better fit the experimental data: for the O K-edge and U L_3-edge spectra, we employed a Voigt profile, and for the U M_4-edge, a Gaussian function. In the Supporting Information, Figure S3 presents the effect of the damping factors, and Figures S4−S6 show the effect of the broadening profiles on the simulated spectra.

Polarization Dependence of Calculated Intensities. Synchrotron-based experiments can also handle dichroism in the X-ray regime. Linear dichroism is studied using angle-resolved and polarization-dependent X-ray absorption spectroscopy,[47,100,125] while magnetic circular dichroism has been extensively studied through X-ray magnetic circular dichroism (XMCD).[126,127]

By utilizing the damped response theory, linear dichroism can be explored through the analysis of the components of the complex polarizability tensor ($\alpha_{xx}(\omega)$, $\alpha_{yy}(\omega)$, and $\alpha_{zz}(\omega)$). As we shall see in the following, the breakdown into individual components—or here, due to the symmetry of the system into parallel (σ_{zz}) and perpendicular ($\sigma_{xx+yy} = \sigma_{xx} + \sigma_{yy}$) components with respect to the uranyl bond axis—is helpful to understand the origin of the asymmetries observed experimentally.

In Figure 3, we show the parallel and perpendicular contributions to the total absorption cross section ($\sigma_{xx+yy+zz} = \sigma_{zz} + \sigma_{xx+yy}$) for the edges under investigation, alongside the experimental polarization-dependent spectra,[47,100] in which the angle indicated is the one between the incident light beam and the O−U−O axis in the $Cs_2UO_2Cl_4$ crystal.

The effects of polarization dependence are particularly prominent in the experimental spectra at the O K-edge by Denning et al.[100] and the U L_3-edge by Vitova et al.[47] (Figure 3a−c), which were recorded at greater incidence angles than the ones for the U M_4-edge. For clarity, here, we will compare our results to the experiments under grazing and nearly perpendicular light incidence conditions.

For the O K-edge, our analysis finds that transitions **T1** and **T3** are dominated by perpendicularly polarized components with respect to the O−U−O axis, whereas **T2** was found to exhibit parallel polarization, in agreement with the experiment. For the L_3-edge, we observe that **T8** is completely dominated by perpendicularly polarized components. For **T9**, the spectrum shows non-negligible contributions from the parallel component, which we consider to be consistent with the observation by Vitova et al.[47] that angle dependence shifts the U L_3-edge absorption edge to the right when incoming light is parallel to the O−U−O axis.

Finally, for the U M_4-edge (Figure 3b), a strong angular dependence in the white line (**T4**) is observed, and as for the other edges, the perpendicular components are the major contributors to the intensity. For **T5**, we see that the parallel component contributes proportionally more to the total signal, and this trend is accentuated for **T6**, for which we see nearly equal contributions from both components to the total intensity.

Closer Look on the Role of the Equatorial Ligands. Having established that 4c-DR and 2c-TDA can faithfully describe the spectra for the edges under consideration, we can turn to a comparison of the different structural models described in Figure 1 ($UO_2Cl_4^{2-}$, the bare uranyl ion and the uranyl ion embedded onto the equatorial chloride ligands) in order to gain further understanding of the role of the equatorial ligands.

As mentioned above, the core spectra of the bare uranyl ion were not only investigated by Polly et al.[83] but also by Sergentu et al.[81] The embedded uranyl model ($UO_2^{2+}@Cl_4^{4-}$), on the other hand, has only been previously investigated for the valence excited state[97] and shown to yield a rather good description of the low-lying states of $UO_2Cl_4^{2-}$ in $Cs_2UO_2Cl_4$.

Given the high sensitivity of core excited states to the description of the environment around the absorbing sites, it remains to be seen to which extent the embedded model can faithfully reproduce the reference ($UO_2Cl_4^{2-}$) calculations. In this respect, an interesting feature to track is the relative positions of the different peak maxima as well as their relative intensities and how these compare to the experimental ones.

At the O K-edge (Figure 4, top), there are rather small differences between the energy shifts (less than 1 eV) with respect to the experiment among the three simulations. This is in line with a systematic error in the calculations due to the shortcomings in describing relaxation due to the creation of the core hole, mentioned in the previous section.

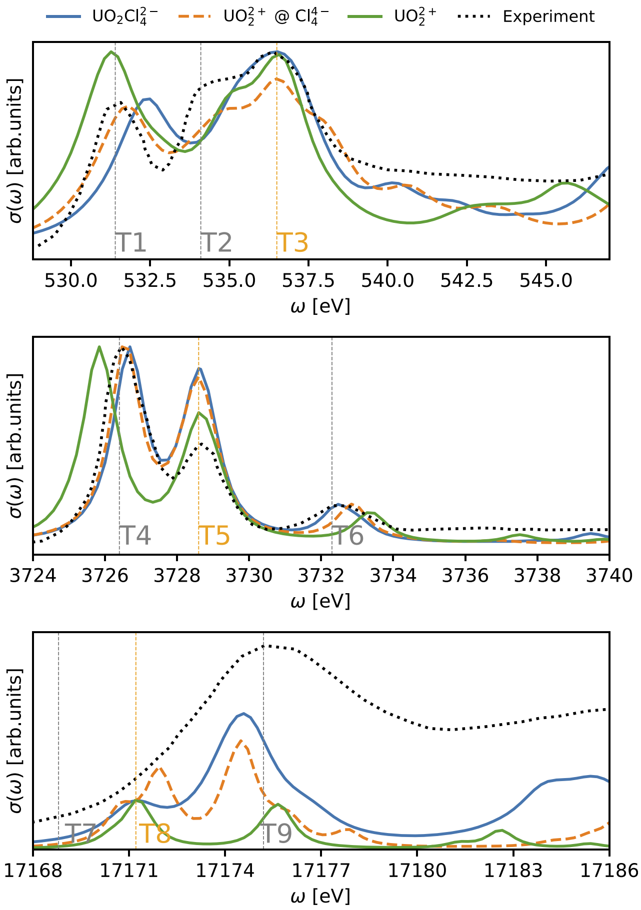

Figure 4. From top to bottom: comparison of the 4c-DR XAS spectra at the oxygen K-edge and uranium M_4- and L_3-edges of UO_2^{2+}, $UO_2^{2+}@Cl_4^{4-}$, and $UO_2Cl_4^{2-}$. Experimental data at the O K-edge in $Cs_2UO_2Cl_4$ (digitized with permission from Denning et al.[100] Copyright 2002 AIP Publishing) and for the U M_4- and L_3-edges (digitized from Vitova et al.[47] Copyright 2015 American Chemical Society).

For the intensities, on the other hand, we observe for **T1** that the bare uranyl model shows a significant overestimation. Intensities for the reference and embedded models on the

Table 2. U M_4-Edge Peak Positions and Differences (in eV) from Theoretical Molecular (4c-DR, RASPT2, and RASSCF) and Finite-Difference (FDMNES) Calculations and the Experiment (HERFD)

		peak positions			differences		
method	system	T4	T5	T6	T5 − T4	T6 − T4	T6 − T5
4c-DR	UO_2^{2+}	3689.0	3691.8	3696.5	2.8	7.5	4.7
RASSCF[81]	UO_2^{2+}	3750.1	3752.4	3758.0	2.3	7.9	5.6
RASSCF[a,83]	UO_2^{2+}	3748.0	3750.1	3755.7	2.1	7.7	5.6
RASSCF[b,83]	UO_2^{2+}	3750.6	3753.1	3759.4	2.5	8.8	6.3
RASPT2[b,83]	UO_2^{2+}	3746.1	3748.8	3755.1	2.7	9.0	6.3
4c-DR	$UO_2^{2+}@Cl_4^{4-}$	3690.1	3692.0	3696.2	1.9	6.1	4.2
4c-DR	$UO_2Cl_4^{2-}$	3689.5	3691.4	3695.3	1.9	5.8	3.9
FDMNES[128]	$Cs_2UO_2Cl_4$	3726.9	3729.3	3732.9	2.4	6.0	3.6
HERFD[47]	$Cs_2UO_2Cl_4$	3726.4	3728.6	3732.3	2.2	5.9	3.7

[a] Active space: 3d (σ_u,π_u)/5f. [b] 3d/5f.

other hand are very similar to one another, though the maximum for the embedded model is slightly shifted to lower energies. For **T2** and **T3**, the different models show an overall good agreement with each other, and a finer comparison is more difficult than that for **T1** in view of the overlapping contributions from different transitions to the final spectrum. We note, however, that for the bare and embedded uranyl, the feature corresponding to the parallel component (**T2**, see Figure 3a) appears slightly more shifted to the lower energies than that for uranyl tetrachloride, resulting in the asymmetry in the region between **T2** and **T3**. We note that experimentally, the intensity of absorption between **T2** and **T3** is rather sensitive to polarization[100] (see Figure 3a).

The simulations at the U M_4-edge spectra (Figure 4, middle) show an even better agreement between the embedding calculations and the reference ones than those at the O K-edge spectra, with both simulations reproducing the experiment rather well for all peaks. However, if the splitting between **T4** and **T5** is very well reproduced, we see that for the embedding calculation of **T6**, there is a slight shift in the peak maximum to higher energies compared both to the experiment and to the reference model, while the latter two show again very good agreement. For bare uranyl, on the other hand, we see a fairly significant overestimation of both **T4−T5** and **T5−T6** peak shifts compared to the reference model.

The ability of a theoretical model to accurately characterize peak splittings is of importance for the U M_4-edge, since the solid-state community commonly attributes variations in peak splitting between the main feature and the satellite $5f_\sigma^*$ in actinyl spectra to changes in overlap-driven covalency from variations in the An−O bond length, as suggested in the works of Kvashnina and Butorin[33] and Vitova and collaborators.[47,48] This is somewhat at odds with the analysis based on ab initio simulations, such as those by Sergentu et al.[81] and also Polly et al.,[83] which claim that there is not a clear correlation between those and the observed splitting in this spectrum. The natural localized molecular orbital (NLMO) analysis by Sergentu et al.[81] found a significant decrease in the σ covalency in the excited states of the actinyl absorption spectra at the M_4-edges of PuO_2^{2+}, NpO_2^{2+}, and UO_2^{2+}, in a trend that opposes the one observed in their ground states. Therefore, they were able to highlight the limitations of the previous interpretations of these spectra, by showing that the orbitals of the ground state should not be used as the sole guide in interpreting these actinyl spectra.

In Table 2, we present the peak positions and splitting of the U M_4-edge spectra obtained from experiments by Vitova et al.[47] and predicted by molecular ab initio calculations (Sergentu et al.,[81] Polly et al.,[83] and this work) as well as ab initio finite-difference calculations by Amidani et al.[128] using the FDMNES code.[129,130]

As previously discussed, the shortcomings of 4c-DR calculations in including relaxation result in excitation energies that are too low compared to the experiment or RASSCF/RASPT2. The peak splitting values, on the other hand, indicate that despite better accounting for orbital relaxation, RASSCF and RASPT2 calculations do not compare more favorably to the experiment than 4c-DR calculations relying on TD-DFT/CAM-B3LYP, and changing the size of the active space changes peak positions by a few electronvolts but peak splittings by a few tenths of electronvolts. Relaxation aside, the comparable performance of CAM-B3LYP with respect to RASSCF/RASPT2 is in line with previous benchmark studies[131,132] and has been explained in terms of its good ability to minimize self-interaction errors that plague other functionals, so that excitation energies can be reliably obtained with it, including for charge-transfer excitations.[96,133]

Taken as a whole, we attribute the overestimation of peak splittings shown for all of these calculations to the lack of equatorial ligands, since when these are included (embedding or supermolecular 4c-DR calculations), we achieve very good agreement with the experiment, especially for the **T6−T4** and **T6−T5** splittings. It is interesting to note that the RASPT2 approach, which one could expect to improve upon RASSCF, ends up further overestimating peak splittings. This could be due to a poor balance between orbital relaxation and the amount of dynamic correlation recovered with second-order perturbation theory, possibly coupled with the lack of equatorial ligands in the calculations.

Coming back to the **T6−T4** and **T6−T5** splittings, we observe slight differences between the embedding and supermolecule calculations, which would suggest that orbital interactions are somewhat more important for **T6** than that for **T4** or **T5**, since the **T5−T4** splitting for both models is essentially the same, whereas it increases slightly for **T6−T5**.

In the embedding calculation, apart from the symmetry breaking with respect to linear symmetry that allows for some mixing of the ϕ, δ spinors,[134] the chloride ligands are included only through the embedding potential, which represents an effective interaction. As a result, by construction, the electrostatic interaction component of the embedding potential remains the dominant contribution. Therefore, the differences between the two models can be traced back to the lack of such interaction in the bare uranyl case.

The importance of electrostatic interactions, as well as the sensitivity of the actinyl electronic structure to these, has been addressed in more detail in our previous investigations of actinyl chlorides. First, for the valence states of uranyl,[97] we also considered a simple model with negative point charges placed in the positions of the chlorides and found that the valence excited states were in better agreement with uranyl tetrachloride than bare uranyl, though this point-charge embedding model still showed a poorer performance than the FDE ($UO_2^{2+}@Cl_4^{4-}$) model. Second, in the investigation[134] of f−f transitions in $NpO_2Cl_4^{2-}$, we considered an embedding model equivalent to the one used here ($NpO_2^{2+}@Cl_4^{4-}$), as well as a variant in which the density of the chlorides was not relaxed in the presence of the neptunyl ion, and a point-charge embedding model. We showed that the embedded model without relaxation of the chloride ligands' density yielded results that were comparable to the point-charge one and did not reproduce the spectra of neptunyl chloride as well as $NpO_2^{2+}@Cl_4^{4-}$.

From the above considerations and our current results, we argue that substantial contributions to the shifts in the U M_4-edge peak position in Table 2 can be attributed to electrostatic interactions with the equatorial ligands. It would be interesting to investigate to which extent that would hold for the core spectra of other actinyls and that for ligands other than halides, but such a study is beyond the scope of this work. In the case of other actinyls, which may present a multireference ground state, it will be in general necessary to replace the DFT treatment of the active subsystem by a wavefunction-based method, but as we have shown for neptunyl,[134] that does not pose particular issues for the FDE calculations.

At the U L_3-edge (Figure 4), we have obtained the same results as South et al.[57] for the uranyl ion, which presents a second feature (**T9**) quite shifted to the right, therefore not being compatible with any spectra recorded at this absorption edge for uranium-containing species. The embedding calculation presents a broader and more intense **T8** feature, with **T9** resembling rather well that of the reference model.

We note that here, we have not considered more sophisticated models in which the crystal environment in $Cs_2UO_2Cl_4$ beyond the equatorial chloride ligands (structure **a** in Figure 1) is included in the embedding potential. This is due to the fact that in our previous investigation of valence excited states,[97] we have compared the results for the embedded uranyl tetrachloride model employed here ($UO_2^{2+}@Cl_4^{4-}$) with others in which the effect of the rest of the crystal is taken into account by embedding potentials. In these potentials, we defined a frozen density region, consisting of equatorial chlorides plus 20 uranyl tetrachloride and 90 cesium atoms surrounding the central uranyl unit; beyond this quantum mechanical region, an array of point charges was used to simulate the long-range electrostatics in the crystal.

For a first model, in which all subsystem densities but that of the chloride equatorial ligands were kept frozen, we observed for the 12 lowest valence excited states changes in excitation energies that differed at most by 0.015 eV (with discrepancies being on average of about 0.0075 eV, in absolute value) from the $UO_2^{2+}@Cl_4^{4-}$ model. Furthermore, when the density of the nearest cesium atoms was also relaxed, the excitation energies only changed by around 0.002−0.004 eV.

As discussed by Gomes et al.,[97] the physical process behind these changes is that the effect of the crystal environment lowers the energies of both occupied and virtual orbitals by roughly the same amounts. In addition to that, the energies of occupied valence[97,134,135] and core levels[136] are shifted by essentially the same amount as by the environment. With that, relative measures such as excitation energies turn out to be weakly affected by the environment.

Apart from the arguments above, we consider the suitability of our uranyl tetrachloride models to be further supported by the good agreement between all of our peak splittings for the uranyl tetrachloride models and those from Amidani et al.,[128] obtained with the FDMNES method.

In the latter calculation, all atoms within a 6 Å radius around the absorbing uranium atom in the $Cs_2UO_2Cl_4$ crystal are taken into account, which is in between our models without and with accounting for the rest of the crystal. We note that the FDMNES calculations are also based on DFT and account for scalar and spin−orbit relativistic effects but differ qualitatively from ours in that they include the effect of core-hole creation through a screening parameter. With that, their absolute peak positions are also in good agreement with the experiment, while ours require a shift in energy to be compared to the experiment.

For ionizations, on the other hand, long-range interactions with the environment are important[97,135,136] and require the use of more sophisticated structural models. We shall address the ionizations of uranyl in $Cs_2UO_2Cl_4$ in a separate publication.

■ CONCLUSIONS

We have carried out an evaluation of relativistic quantum chemistry approaches for the calculation of excitation energies at the oxygen K-edge and uranium M_4- and L_3-edges for the $UO_2Cl_4^{2-}$ system, which makes up the $Cs_2UO_2Cl_4$ crystal. Besides calculating on this system, we have also investigated the performance of two other structural models, the bare uranyl ion and the uranyl ion embedded (via the frozen density embedding (FDE) method) in an environment made up of chloride equatorial ligands.

For these excitation energies, the use of the Coulomb-attenuating functional CAM-B3LYP in four-component damped response simulations produced results that were consistent with the features observed in both conventional XANES and HERFD experiments. Additionally, through the analysis of natural transition orbitals (NTOs) obtained from equivalent two-component time-dependent DFT calculations, we showed that the O K-edge spectra primarily provided insights into the low-lying antibonding states of π_u^*, σ_u^*, and π_g^* symmetries centered in the uranyl unit. In contrast, the lowest energy orbitals accessed at the U M_4 and U L_3 absorption edges are the uranium $5f\phi_u/\delta_u$ and $6d\delta_g/\pi_g$ nonbonding orbitals. These observations are in line with previous investigations.

We have determined that the bare uranyl model shows significant changes in spectral profiles in comparison to structural models containing equatorial ligands, notably in terms of relative intensities but also to some extent with respect to relative peak positions. This is seen not only for the uranium edges, to which the equatorial ligands are attached, but also for the oxygen K-edge.

In the soft and tender X-ray regime (O K-edge and U M_4-edge), we have observed that our simulations for the embedded model yield both excitation energies and intensities in very good agreement with those obtained for the $UO_2Cl_4^{2-}$ ion, though in the hard X-ray regime (U L_3-edge), this approximate model still performs well but deviates more significantly from the results obtained for the anion.

In conclusion, our study has provided valuable insights into the impact of equatorial ligands on the X-ray absorption spectra of the uranyl ion. Our findings emphasize the limitations of relying solely on a structural model consisting of either the bare uranyl ion or the ground-state structure of the uranyl site, as these models do not accurately account for the influence of the equatorial ligands on peak positions.

Furthermore, our work demonstrates the potential of using accurate embedded models, such as those that can be constructed with frozen density embedding, to semiquantitatively simulate actinyl core spectra. FDE-based embedding models have already been employed with multireference wavefunction-based treatment for the active subsystem, to treat systems that are challenging for DFT or other single-reference methods, though not yet for the core spectra of actinides employing accurate ab initio relativistic quantum chemistry methods.

ASSOCIATED CONTENT

Supporting Information

The data corresponding to the calculations of this paper are available at https://doi.org/10.5281/zenodo.7632750. The Supporting Information is available free of charge at https://pubs.acs.org/doi/10.1021/acs.inorgchem.3c01302.

> Further theoretical background on damped response theory and frozen density embedding; comparison of two- and four-component calculations for uranyl tetrachloride; assessment of the effect of the damping parameter used in the damped response theory calculations; comparison of the effect of different broadening functions on spectral shapes; and comparison of the differences in energy shifts with respect to the experiment for the bare and embedded uranyl models and uranyl tetrachloride (PDF)

AUTHOR INFORMATION

Corresponding Author

André Severo Pereira Gomes − *Univ. Lille, CNRS, UMR 8523-PhLAM-Physique des Lasers Atomes et Molécules, F-59000 Lille, France;* orcid.org/0000-0002-5437-2251; Email: andre.gomes@univ-lille.fr

Author

Wilken Aldair Misael − *Univ. Lille, CNRS, UMR 8523-PhLAM-Physique des Lasers Atomes et Molécules, F-59000 Lille, France;* orcid.org/0000-0002-4138-3517

Complete contact information is available at:
https://pubs.acs.org/10.1021/acs.inorgchem.3c01302

Notes

The authors declare no competing financial interest.

ACKNOWLEDGMENTS

The authors acknowledge discussions with Dr. Valérie Vallet (Université de Lille) on carrying out the analysis of natural transition orbitals and on the manuscript. W.A.M. acknowledges helpful discussions with Dr. Patrick Norman (KTH) on general aspects of response theory. The authors acknowledge support from the Franco-German project CompRIXS (Agence nationale de la recherche ANR-19-CE29-0019, Deutsche Forschungsgemeinschaft JA 2329/6-1), PIA ANR project CaPPA (ANR-11-LABX-0005-01), I-SITE ULNE projects OVERSEE and MESONM International Associated Laboratory (LAI) (ANR-16-IDEX-0004), the French Ministry of Higher Education and Research, region Hauts de France council and European Regional Development Fund (ERDF) project CPER CLIMIBIO, and the French national supercomputing facilities (grants DARI A0090801859, A0110801859, and A0130801859).

REFERENCES

(1) Crossland, I. *Nuclear Fuel Cycle Science and Engineering*; Elsevier, 2012.

(2) Veliscek-Carolan, J. Separation of actinides from spent nuclear fuel: A review. *J. Hazard. Mater.* **2016**, *318*, 266−281.

(3) Mathur, J. N.; Murali, M.; Nash, K. Actinide partitioning—a review. *Solvent Extr. Ion Exch.* **2001**, *19*, 357−390.

(4) Hu, Y.; Shen, Z.; Li, B.; Tan, X.; Han, B.; Ji, Z.; Wang, J.; Zhao, G.; Wang, X. State-of-the-art progress for the selective crystallization of actinides, synthesis of actinide compounds and their functionalization. *J. Hazard. Mater.* **2022**, *426*, No. 127838.

(5) De Jesus, K.; Rodriguez, R.; Baek, D.; Fox, R.; Pashikanti, S.; Sharma, K. Extraction of lanthanides and actinides present in spent nuclear fuel and in electronic waste. *J. Mol. Liq.* **2021**, *336*, No. 116006.

(6) Denecke, M. A.; Bryan, N.; Kalmykov, S.; Morris, K.; Quinto, F. *Experimental and Theoretical Approaches to Actinide Chemistry*; Wiley Online Books, 2018.

(7) Pavlyuk, A. O.; Kotlyarevskii, S. G.; Kan, R. I.; Volkova, A. G.; Yapaskurt, V. O.; Zakharova, E. V.; Shiryaev, A. A. Actinides and fission products in reactor graphite after loss-of-flow accident. *npj Mater. Degrad.* **2022**, *6*, No. 23.

(8) Van der Meeren, A.; Angulo, J. F.; Bohand, S.; Griffiths, N. M. A quick and simple in vitro assay to predict bioavailability of actinides following accidental exposure. *Toxicol. In Vitro* **2019**, *58*, 142−149.

(9) Grambow, B.; Nitta, A.; Shibata, A.; Koma, Y.; Utsunomiya, S.; Takami, R.; Fueda, K.; Ohnuki, T.; Jegou, C.; Laffolley, H.; Journeau, C. Ten years after the NPP accident at Fukushima: review on fuel debris behavior in contact with water. *J. Nucl. Sci. Technol.* **2022**, *59*, 1−24.

(10) Hu, K.-Q.; Huang, Z.-W.; Zhang, Z.-H.; Mei, L.; Qian, B.-B.; Yu, J.-P.; Chai, Z.-F.; Shi, W.-Q. Actinide-Based Porphyrinic MOF as a Dehydrogenation Catalyst. *Chem.—Eur. J.* **2018**, *24*, 16766−16769.

(11) Leduc, J.; Frank, M.; Jürgensen, L.; Graf, D.; Raauf, A.; Mathur, S. Chemistry of actinide centers in heterogeneous catalytic transformations of small molecules. *ACS Catal.* **2019**, *9*, 4719−4741.

(12) Dennett, C. A.; Poudel, N.; Simmonds, P. J.; Tiwari, A.; Hurley, D. H.; Gofryk, K. Towards actinide heterostructure synthesis and science. *Nat. Commun.* **2022**, *13*, No. 2221.

(13) Abney, C. W.; Mayes, R. T.; Saito, T.; Dai, S. Materials for the recovery of uranium from seawater. *Chem. Rev.* **2017**, *117*, 13935−14013.

(14) Parker, B. F.; Zhang, Z.; Rao, L.; Arnold, J. An overview and recent progress in the chemistry of uranium extraction from seawater. *Dalton Trans.* **2018**, *47*, 639−644.

(15) Ji, S.; Su, M.; Liao, C.; Ma, S.; Wang, Z.; Shih, K.; Chang, C.-K.; Lee, J.-F.; Chan, T.-S.; Li, Y. Synchrotron x-ray spectroscopy investigation of the Ca1- xLnxZrTi2- x (Al, Fe) xO7 zirconolite ceramics (Ln = La, Nd, Gd, Ho, Yb). *J. Am. Ceram. Soc.* **2020**, *103*, 1463−1475.

(16) Vallejo, K. D.; Kabir, F.; Poudel, N.; Marianetti, C.; Hurley, D. H.; Simmonds, P.; Dennett, C. A.; Gofryk, K. Advances in actinide thin films: synthesis, properties, and future directions. *Rep. Prog. Phys.* **2022**, *85*, No. 123101.

(17) Zhai, B.; Tian, Q.; Li, N.; Yan, M.; Henderson, M. J. SAXS study of the formation and structure of polynuclear thorium (IV) colloids and thorium dioxide nanoparticles. *J. Synchrotron Radiat.* **2022**, *29*, 281.

(18) Pallares, R. M.; Abergel, R. J. Transforming lanthanide and actinide chemistry with nanoparticles. *Nanoscale* **2020**, *12*, 1339−1348.

(19) Ion, R.-M.; Sorescu, A.-A.; Nuta, A. *Handbook of Greener Synthesis of Nanomaterials and Compounds*; Elsevier, 2021; pp 355−388.

(20) Bonato, L.; Virot, M.; Dumas, T.; Mesbah, A.; Dalodière, E.; Blanco, O. D.; Wiss, T.; Le Goff, X.; Odorico, M.; Prieur, D.; et al. Probing the local structure of nanoscale actinide oxides: a comparison between PuO 2 and ThO 2 nanoparticles rules out PuO 2+ x hypothesis. *Nanoscale Adv.* **2020**, *2*, 214−224.

(21) Denning, R. G. Electronic structure and bonding in actinyl ions and their analogs. *J. Phys. Chem. A* **2007**, *111*, 4125−4143.

(22) Lv, B.; Qian, T.; Ding, H. Angle-resolved photoemission spectroscopy and its application to topological materials. *Nat. Rev. Phys.* **2019**, *1*, 609−626.

(23) Sedigh Rahimabadi, P.; Khodaei, M.; Koswattage, K. R. Review on applications of synchrotron-based X-ray techniques in materials characterization. *X-Ray Spectrom.* **2020**, *49*, 348−373.

(24) Wernet, P. Chemical interactions and dynamics with femtosecond X-ray spectroscopy and the role of X-ray free-electron lasers. *Philos. Trans. R. Soc., A* **2019**, *377*, No. 20170464.

(25) Golubev, N. V.; Vaníček, J.; Kuleff, A. I. Core-valence attosecond transient absorption spectroscopy of polyatomic molecules. *Phys. Rev. Lett.* **2021**, *127*, No. 123001.

(26) Stöhr, J. *NEXAFS Spectroscopy*; Springer Science & Business Media, 1992; Vol. *25*.

(27) Van Bokhoven, J. A.; Lamberti, C. *X-ray Absorption and X-ray Emission Spectroscopy: Theory and Applications*; John Wiley & Sons, 2016; Vol. *1*.

(28) Iwasawa, Y.; Asakura, K.; Tada, M. *XAFS Techniques for Catalysts, Nanomaterials, and Surfaces*; Springer, 2017.

(29) Stöhr, J. What are X-rays, Anyway: A Modern View of the Nature of Light and its Implications for the Future of X-ray Science. *Synchrotron Radiat. News* **2019**, 48.

(30) Vitova, T.; Pidchenko, I.; Fellhauer, D.; Pruessmann, T.; Bahl, S.; Dardenne, K.; Yokosawa, T.; Schimmelpfennig, B.; Altmaier, M.; Denecke, M.; et al. Exploring the electronic structure and speciation of aqueous and colloidal Pu with high energy resolution XANES and computations. *Chem. Commun.* **2018**, *54*, 12824−12827.

(31) Zegke, M.; Zhang, X.; Pidchenko, I.; Hlina, J. A.; Lord, R. M.; Purkis, J.; Nichol, G. S.; Magnani, N.; Schreckenbach, G.; Vitova, T.; et al. Differential uranyl (v) oxo-group bonding between the uranium and metal cations from groups 1, 2, 4, and 12; a high energy resolution X-ray absorption, computational, and synthetic study. *Chem. Sci.* **2019**, *10*, 9740−9751.

(32) Popa, K.; Prieur, D.; Manara, D.; Naji, M.; Vigier, J.-F.; Martin, P. M.; Blanco, O. D.; Scheinost, A. C.; Prü*β*mann, T.; Vitova, T.; et al. Further insights into the chemistry of the Bi-U-O system. *Dalton Trans.* **2016**, *45*, 7847−7855.

(33) Kvashnina, K. O.; Butorin, S. M. High-energy resolution X-ray spectroscopy at actinide M 4, 5 and ligand K edges: what we know, what we want to know, and what we can know. *Chem. Commun.* **2022**, *58*, 327−342.

(34) Vitova, T.; Kvashnina, K.; Nocton, G.; Sukharina, G.; Denecke, M.; Butorin, S.; Mazzanti, M.; Caciuffo, R.; Soldatov, A.; Behrends, T.; Geckeis, H. High energy resolution X-ray absorption spectroscopy study of uranium in varying valence states. *Phys. Rev. B: Condens. Matter Mater. Phys.* **2010**, *82*, No. 235118.

(35) Lindroth, E.; Calegari, F.; Young, L.; Harmand, M.; Dudovich, N.; Berrah, N.; Smirnova, O. Challenges and opportunities in attosecond and XFEL science. *Nat. Rev. Phys.* **2019**, *1*, 107−111.

(36) Zimina, A.; Dardenne, K.; Denecke, M. A.; Grunwaldt, J.; Huttel, E.; Lichtenberg, H.; Mangold, S.; Pruessmann, T.; Rothe, J.; Steininger, R.; Vitova, T. The CAT-ACT Beamline at ANKA: A new high energy X-ray spectroscopy facility for CATalysis and ACTinide research. *J. Phys.* **2016**, *712*, No. 012019.

(37) Scheinost, A. C.; Claussner, J.; Exner, J.; Feig, M.; Findeisen, S.; Hennig, C.; Kvashnina, K. O.; Naudet, D.; Prieur, D.; Rossberg, A.; et al. ROBL-II at ESRF: a synchrotron toolbox for actinide research. *J. Synchrotron Radiat.* **2021**, *28*, 333−349.

(38) Caciuffo, R.; Lander, G. H. X-ray synchrotron radiation studies of actinide materials. *J. Synchrotron Radiat.* **2021**, *28*, 1692−1708.

(39) Shi, W.-Q.; Yuan, L.-Y.; Wang, C.-Z.; Wang, L.; Mei, L.; Xiao, C.-L.; Zhang, L.; Li, Z.-J.; Zhao, Y.-L.; Chai, Z.-F.Exploring Actinide Materials Through Synchrotron Radiation Techniques. *Synchrotron Radiation in Materials Science: Light Sources, Techniques, and Applications*; John Wiley & Sons, Inc., 2018; Vol. *2*, pp 389−509.

(40) Rothe, J.; Altmaier, M.; Dagan, R.; Dardenne, K.; Fellhauer, D.; Gaona, X.; González-Robles Corrales, E.; Herm, M.; Kvashnina, K. O.; Metz, V.; et al. Fifteen years of radionuclide research at the KIT synchrotron source in the context of the nuclear waste disposal safety case. *Geosciences* **2019**, *9*, No. 91.

(41) Husar, R.; Dumas, T.; Schlegel, M. L.; Schlegel, D.; Guillaumont, D.; Solari, P.-L.; Moisy, P. X-ray absorption spectroscopy and actinide electrochemistry: a setup dedicated to radioactive samples applied to neptunium chemistry. *J. Synchrotron Radiat.* **2022**, *29*, 1−10.

(42) Vitova, T.; Denecke, M.; Göttlicher, J.; Jorissen, K.; Kas, J.; Kvashnina, K.; Prüßmann, T.; Rehr, J.; Rothe, J. Actinide and lanthanide speciation with high-energy resolution X-ray techniques. *J. Phys.* **2013**, *430*, No. 012117.

(43) Kvashnina, K.; Kvashnin, Y.; Butorin, S. Role of resonant inelastic X-ray scattering in high-resolution core-level spectroscopy of actinide materials. *J. Electron Spectrosc. Relat. Phenom.* **2014**, *194*, 27−36.

(44) Willmott, P. *An Introduction to Synchrotron Radiation: Techniques and Applications*; John Wiley & Sons, 2019.

(45) Nocton, G.; Mazzanti, M.Coordination Chemistry of Actinides. *Lanthanides and Actinides, The: Synthesis, Reactivity, Properties and Applications*; World Scientific Europe Ltd., 2021; p 149.

(46) McSkimming, A.; Su, J.; Cheisson, T.; Gau, M. R.; Carroll, P. J.; Batista, E. R.; Yang, P.; Schelter, E. J. Coordination chemistry of a strongly-donating hydroxylamine with early actinides: An investigation of redox properties and electronic structure. *Inorg. Chem.* **2018**, *57*, 4387−4394.

(47) Vitova, T.; Green, J. C.; Denning, R. G.; Löble, M.; Kvashnina, K.; Kas, J. J.; Jorissen, K.; Rehr, J. J.; Malcherek, T.; Denecke, M. A. Polarization dependent high energy resolution X-ray absorption study of dicesium uranyl tetrachloride. *Inorg. Chem.* **2015**, *54*, 174−182.

(48) Vitova, T.; Pidchenko, I.; Fellhauer, D.; Bagus, P. S.; Joly, Y.; Pruessmann, T.; Bahl, S.; Gonzalez-Robles, E.; Rothe, J.; Altmaier, M.; et al. The role of the 5f valence orbitals of early actinides in chemical bonding. *Nat. Commun.* **2017**, *8*, No. 16053.

(49) Gibson, J. K.; de Jong, W. A. *Experimental and Theoretical Approaches to Actinide Chemistry*; John Wiley & Sons, 2018.

(50) Ganguly, G.; Sergentu, D.-C.; Autschbach, J. Ab Initio Analysis of Metal-Ligand Bonding in An (COT) 2 with An= Th, U in Their Ground-and Core-Excited States. *Chem.—Eur. J.* **2020**, *26*, 1776−1788.

(51) Norman, P.; Dreuw, A. Simulating X-ray spectroscopies and calculating core-excited states of molecules. *Chem. Rev.* **2018**, *118*, 7208−7248.

(52) Besley, N. A. Modeling of the spectroscopy of core electrons with density functional theory. *Wiley Interdiscip. Rev.: Comput. Mol. Sci.* **2021**, *11*, No. e1527.

(53) Zheng, X.; Cheng, L. Performance of delta-coupled-cluster methods for calculations of core-ionization energies of first-row elements. *J. Chem. Theory Comput.* **2019**, *15*, 4945−4955.

(54) Wenzel, J.; Holzer, A.; Wormit, M.; Dreuw, A. Analysis and comparison of CVS-ADC approaches up to third order for the calculation of core-excited states. *J. Chem. Phys.* **2015**, *142*, No. 214104.

(55) Vidal, M. L.; Feng, X.; Epifanovsky, E.; Krylov, A. I.; Coriani, S. New and efficient equation-of-motion coupled-cluster framework for core-excited and core-ionized states. *J. Chem. Theory Comput.* **2019**, *15*, 3117−3133.

(56) Sen, S.; Shee, A.; Mukherjee, D. Inclusion of orbital relaxation and correlation through the unitary group adapted open shell coupled cluster theory using non-relativistic and scalar relativistic Hamiltonians to study the core ionization potential of molecules containing light to medium-heavy elements. *J. Chem. Phys.* **2018**, *148*, No. 054107.

(57) South, C.; Shee, A.; Mukherjee, D.; Wilson, A. K.; Saue, T. 4-Component relativistic calculations of L 3 ionization and excitations for the isoelectronic species UO 2 2+, OUN+ and UN 2. *Phys. Chem. Chem. Phys.* **2016**, *18*, 21010−21023.

(58) Park, J. W.; Al-Saadon, R.; MacLeod, M. K.; Shiozaki, T.; Vlaisavljevich, B. Multireference electron correlation methods: Journeys along potential energy surfaces. *Chem. Rev.* **2020**, *120*, 5878−5909.

(59) Lischka, H.; Nachtigallova, D.; Aquino, A. J.; Szalay, P. G.; Plasser, F.; Machado, F. B.; Barbatti, M. Multireference approaches for excited states of molecules. *Chem. Rev.* **2018**, *118*, 7293−7361.

(60) Norman, P.; Ågren, H. Geometry optimization of core electron excited molecules. *J. Mol. Struct.: THEOCHEM* **1997**, *401*, 107−115.

(61) Gulania, S.; Kjønstad, E. F.; Stanton, J. F.; Koch, H.; Krylov, A. I. Equation-of-motion coupled-cluster method with double electron-attaching operators: Theory, implementation, and benchmarks. *J. Chem. Phys.* **2021**, *154*, No. 114115.

(62) Vidal, M. L.; Pokhilko, P.; Krylov, A. I.; Coriani, S. Equation-of-motion coupled-cluster theory to model L-edge x-ray absorption and photoelectron spectra. *J. Phys. Chem. Lett.* **2020**, *11*, 8314−8321.

(63) Pavošević, F.; Rousseau, B. J.; Hammes-Schiffer, S. Multicomponent orbital-optimized perturbation theory methods: Approaching coupled cluster accuracy at lower cost. *J. Phys. Chem. Lett.* **2020**, *11*, 1578−1583.

(64) Krykunov, M.; Ziegler, T. Self-consistent formulation of constricted variational density functional theory with orbital relaxation. implementation and applications. *J. Chem. Theory Comput.* **2013**, *9*, 2761−2773.

(65) Saue, T. Relativistic Hamiltonians for chemistry: A primer. *ChemPhysChem* **2011**, *12*, 3077−3094.

(66) Liu, W. Essentials of relativistic quantum chemistry. *J. Chem. Phys.* **2020**, *152*, No. 180901.

(67) Dyall, K. G.; Fægri, K., Jr. *Introduction to Relativistic Quantum Chemistry*; Oxford University Press, 2007.

(68) Pyykkö, P. *Advances in Quantum Chemistry*; Elsevier, 1978; Vol. *11*, pp 353−409.

(69) Reiher, M.; Wolf, A. *Relativistic Quantum Chemistry: The Fundamental Theory of Molecular Science*; John Wiley & Sons, 2014.

(70) Thiel, W.; Hummer, G. Methods for computational chemistry. *Nature* **2013**, *504*, 96−97.

(71) Severo Pereira Gomes, A.; Jacob, C. R. Quantum-chemical embedding methods for treating local electronic excitations in complex chemical systems. *Annu. Rep. Sect. C: Phys. Chem.* **2012**, *108*, 222−277.

(72) Jacob, C. R.; Neugebauer, J. Subsystem density-functional theory. *Wiley Interdiscip. Rev.: Comput. Mol. Sci.* **2014**, *4*, 325−362.

(73) Jones, L. O.; Mosquera, M. A.; Schatz, G. C.; Ratner, M. A. Embedding methods for quantum chemistry: applications from materials to life sciences. *J. Am. Chem. Soc.* **2020**, *142*, 3281−3295.

(74) Di Remigio, R.; Bast, R.; Frediani, L.; Saue, T. Four-component relativistic calculations in solution with the polarizable continuum model of solvation: theory, implementation, and application to the group 16 dihydrides H2X (X= O, S, Se, Te, Po). *J. Phys. Chem. A* **2015**, *119*, 5061−5077.

(75) Parmar, P.; Samuels, A.; Clark, A. E. Applications of polarizable continuum models to determine accurate solution-phase thermochemical values across a broad range of cation charge-the case of U (III-VI). *J. Chem. Theory Comput.* **2015**, *11*, 55−63.

(76) Oher, H.; Réal, F.; Vercouter, T.; Vallet, V. Investigation of the Luminescence of [UO2X4] 2-(X= Cl, Br) Complexes in the Organic Phase Using Time-Resolved Laser-Induced Fluorescence Spectroscopy and Quantum Chemical Simulations. *Inorg. Chem.* **2020**, *59*, 5896−5906.

(77) Oher, H.; Ferru, G.; Couston, L.; Berthon, L.; Guillaumont, D.; Réal, F.; Vercouter, T.; Vallet, V. Influence of the First Coordination of Uranyl on Its Luminescence Properties: A Study of Uranyl Binitrate with N, N-Dialkyl Amide DEHiBA and Water. *Inorg. Chem.* **2022**, *61*, 890−901.

(78) Karbowiak, M.; Drozdzynski, J.; Murdoch, K.; Edelstein, N.; Hubert, S. Spectroscopic studies and crystal-field analysis of U3+ ions in RbY2Cl7 single crystals. *J. Chem. Phys.* **1997**, *106*, 3067−3077.

(79) Thouvenot, P.; Hubert, S.; Edelstein, N. Spectroscopic study and crystal-field analysis of Cm 3+ in the cubic-symmetry site of ThO 2. *Phys. Rev. B: Condens. Matter Mater. Phys.* **1994**, *50*, 9715.

(80) Butorin, S. M.; Bauters, S.; Amidani, L.; Beck, A.; Weiss, S.; Vitova, T.; Tougait, O. X-ray spectroscopic study of chemical state in uranium carbides. *J. Synchrotron Radiat.* **2022**, *29*, 295.

(81) Sergentu, D.-C.; Duignan, T. J.; Autschbach, J. Ab initio study of covalency in the ground versus core-excited states and X-ray absorption spectra of actinide complexes. *J. Phys. Chem. Lett.* **2018**, *9*, 5583−5591.

(82) Ramanantoanina, H.; Kuri, G.; Martin, M.; Bertsch, J. Study of electronic structure in the L-edge spectroscopy of actinide materials: UO 2 as an example. *Phys. Chem. Chem. Phys.* **2019**, *21*, 7789−7801.

(83) Polly, R.; Schacherl, B.; Rothe, J.; Vitova, T. Relativistic Multiconfigurational Ab Initio Calculation of Uranyl 3d4f Resonant Inelastic X-ray Scattering. *Inorg. Chem.* **2021**, *60*, 18764−18776.

(84) Sergentu, D.-C.; Autschbach, J. X-ray absorption spectra of f-element complexes: insight from relativistic multiconfigurational wavefunction theory. *Dalton Trans.* **2022**, *51*, 1754−1764.

(85) Sergentu, D.-C.; Autschbach, J. Covalency in actinide(IV) hexachlorides in relation to the chlorine K-edge X-ray absorption structure. *Chem. Sci.* **2022**, *13*, 3194−3207.

(86) Tobin, J. G.; Ramanantoanina, H.; Daul, C.; Roussel, P.; Yu, S.-W.; Nowak, S.; Alonso-Mori, R.; Kroll, T.; Nordlund, D.; Weng, T.-C.; Sokaras, D. Unoccupied electronic structure of actinide dioxides. *Phys. Rev. B: Condens. Matter Mater. Phys.* **2022**, *105*, No. 125129.

(87) Ilton, E. S.; Bagus, P. S. Ligand field effects on the multiplet structure of the U4f XPS of UO2. *Surf. Sci.* **2008**, *602*, 1114−1121.

(88) Ramanantoanina, H.; Kuri, G.; Daul, C.; Bertsch, J. Core electron excitations in U 4+: modelling of the nd 10 5f 2 → nd 9 5f 3 transitions with n = 3, 4 and 5 by ligand field tools and density functional theory. *Phys. Chem. Chem. Phys.* **2016**, *18*, 19020−19031.

(89) Ramanantoanina, H. On the calculation of multiplet energies of three-open-shell 4f 13 5f n 6d 1 electron configuration by LFDFT: modeling the optical spectra of 4f core-electron excitation in actinide compounds. *Phys. Chem. Chem. Phys.* **2017**, *19*, 32481−32491.

(90) Spencer, L. P.; Yang, P.; Minasian, S. G.; et al. Tetrahalide Complexes of the [U(NR)2]2+ Ion: Synthesis, Theory, and Chlorine K-Edge X-ray Absorption Spectroscopy. *J. Am. Chem. Soc.* **2013**, *135*, 2279−2290.

(91) Pidchenko, I.; Kvashnina, K. O.; Yokosawa, T.; Finck, N.; Bahl, S.; Schild, D.; Polly, R.; Bohnert, E.; Rossberg, A.; Göttlicher, J.; et al. Uranium redox transformations after U (VI) coprecipitation with magnetite nanoparticles. *Environ. Sci. Technol.* **2017**, *51*, 2217−2225.

(92) Minasian, S. G.; Keith, J. M.; Batista, E. R.; Boland, K. S.; Clark, D. L.; Conradson, S. D.; Kozimor, S. A.; Martin, R. L.; Schwarz, D. E.; Shuh, D. K.; et al. Determining relative f and d orbital contributions to M-Cl covalency in MCl62-(M = Ti, Zr, Hf, U) and UOCl5-using Cl K-edge X-ray absorption spectroscopy and time-dependent density functional theory. *J. Am. Chem. Soc.* **2012**, *134*, 5586−5597.

(93) Konecny, L.; Vicha, J.; Komorovsky, S.; Ruud, K.; Repisky, M. Accurate X-ray Absorption Spectra near L-and M-Edges from Relativistic Four-Component Damped Response Time-Dependent Density Functional Theory. *Inorg. Chem.* **2022**, 830.

(94) Halbert, L.; Vidal, M. L.; Shee, A.; Coriani, S.; Severo Pereira Gomes, A. Relativistic EOM-CCSD for Core-Excited and Core-Ionized State Energies Based on the Four-Component Dirac−Coulomb (- Gaunt) Hamiltonian. *J. Chem. Theory Comput.* **2021**, *17*, 3583−3598.

(95) Yanai, T.; Tew, D. P.; Handy, N. C. A new hybrid exchange-correlation functional using the Coulomb-attenuating method (CAM-B3LYP). *Chem. Phys. Lett.* **2004**, *393*, 51−57.

(96) Tecmer, P.; Bast, R.; Ruud, K.; Visscher, L. Charge-Transfer Excitations in Uranyl Tetrachloride ([UO2Cl4] 2-): How Reliable are Electronic Spectra from Relativistic Time-Dependent Density Functional Theory? *J. Phys. Chem. A* **2012**, *116*, 7397−7404.

(97) Gomes, A. S. P.; Jacob, C. R.; Réal, F.; Visscher, L.; Vallet, V. Towards systematically improvable models for actinides in condensed phase: the electronic spectrum of uranyl in Cs 2 UO 2 Cl 4 as a test case. *Phys. Chem. Chem. Phys.* **2013**, *15*, 15153−15162.

(98) Réal, F.; Vallet, V.; Marian, C.; Wahlgren, U. Theoretical investigation of the energies and geometries of photoexcited uranyl (VI) ion: A comparison between wave-function theory and density functional theory. *J. Chem. Phys.* **2007**, *127*, No. 214302.

(99) Oher, H.; Vercouter, T.; Réal, F.; Shang, C.; Reiller, P. E.; Vallet, V. Influence of Alkaline Earth Metal Ions on Structures and Luminescent Properties of Na m M n UO2 (CO3) 3 (4-m-2 n)-(M= Mg, Ca; m, n= 0-2): Time-Resolved Fluorescence Spectroscopy and Ab Initio Studies. *Inorg. Chem.* **2020**, *59*, 15036−15049.

(100) Denning, R. G.; Green, J.; Hutchings, T.; Dallera, C.; Tagliaferri, A.; Giarda, K.; Brookes, N.; Braicovich, L. Covalency in the uranyl ion: A polarized x-ray spectroscopic study. *J. Chem. Phys.* **2002**, *117*, 8008−8020.

(101) Jensen, H. J. A.; Bast, R.; Gomes, A. S. P.; Saue, T.; Visscher, L. with contributions from Aucar, I. A.; Bakken, V.; Chibueze, C.; Creutzberg, J.; Dyall, K. G.; Dubillard, S.; Ekström, U.; Eliav, E.; Enevoldsen, T.; Faßhauer, E.; Fleig, T.; Fossgaard, O.; Halbert, L.; Hedegård, E. D.; Helgaker, T.; Helmich-Paris, B.; Henriksson, J.; van Horn, M.; Iliaš, M.; Jacob, C. R.; Knecht, S.; Komorovský, S.; Kullie, O.; Lærdahl, J. K.; Larsen, C. V.; Lee, Y. S.; List, N. H.; Nataraj, H. S.; Nayak, M. K.; Norman, P.; Olejniczak, G.; Olsen, J.; Olsen, J. M. H.; Papadopoulos, A.; Park, Y. C.; Pedersen, J. K.; Pernpointner, M.; Pototschnig, J. V.; di Remigio, R.; Repisky, M.; Ruud, K.; Sałek, P.; Schimmelpfennig, B.; Senjean, B.; Shee, A.; Sikkema, J.; Sunaga, A.; Thorvaldsen, A. J.; Thyssen, J.; van Stralen, J.; Vidal, M. L.; Villaume, S.; Visser, O.; Winther, T.; Yamamoto, S.; Yuan, X. DIRAC, A Relativistic Ab Initio Electronic Structure Program, Release DIRAC22, 2022 (available at http://dx.doi.org/10.5281/zenodo.6010450, see also http://www.diracprogram.org).

(102) Saue, T.; Bast, R.; Gomes, A. S. P.; Jensen, H. J. A.; Visscher, L.; Aucar, I. A.; Di Remigio, R.; Dyall, K. G.; Eliav, E.; Fasshauer, E.; et al. The DIRAC code for relativistic molecular calculations. *J. Chem. Phys.* **2020**, *152*, No. 204104.

(103) Dyall, K. G. Relativistic and nonrelativistic finite nucleus optimized triple-zeta basis sets for the 4 p, 5 p and 6 p elements. *Theor. Chem. Acc.* **2002**, *108*, 335−340.

(104) Dyall, K. G. Relativistic double-zeta, triple-zeta, and quadruple-zeta basis sets for the light elements H-Ar. *Theor. Chem. Acc.* **2016**, *135*, No. 128.

(105) Denning, R.; Snellgrove, T.; Woodwark, D. The electronic structure of the uranyl ion: Part I. The electronic spectrum of Cs2UO2Cl4. *Mol. Phys.* **1976**, *32*, 419−442.

(106) Visscher, L.; Dyall, K. G. Dirac-Fock atomic electronic structure calculations using different nuclear charge distributions. *At. Data Nucl. Data Tables* **1997**, *67*, 207−224.

(107) Watkin, D. J.; Denning, R. G.; Prout, K. Structure of dicaesium tetrachlorodioxouranium (VI). *Acta Crystallogr., Sect. C: Cryst. Struct. Commun.* **1991**, *47*, 2517−2519.

(108) Van Lenthe, Ev.; Snijders, J.; Baerends, E. The zero-order regular approximation for relativistic effects: The effect of spin-orbit coupling in closed shell molecules. *J. Chem. Phys.* **1996**, *105*, 6505−6516.

(109) Lembarki, A.; Chermette, H. Obtaining a gradient-corrected kinetic-energy functional from the Perdew-Wang exchange functional. *Phys. Rev. A* **1994**, *50*, 5328−5331.

(110) Ernzerhof, M.; Scuseria, G. E. Assessment of the Perdew-Burke-Ernzerhof exchange-correlation functional. *J. Chem. Phys.* **1999**, *110*, 5029−5036.

(111) Jacob, C. R.; Beyhan, S. M.; Bulo, R. E.; Gomes, A. S. P.; Götz, A. W.; Kiewisch, K.; Sikkema, J.; Visscher, L. PyADFA scripting framework for multiscale quantum chemistry. *J. Comput. Chem.* **2011**, *32*, 2328−2338.

(112) Zhang, Y.; Biggs, J. D.; Healion, D.; Govind, N.; Mukamel, S. Core and valence excitations in resonant X-ray spectroscopy using restricted excitation window time-dependent density functional theory. *J. Chem. Phys.* **2012**, *137*, No. 194306.

(113) Van Lenthe, E.; Baerends, E. J. Optimized Slater-type basis sets for the elements 1−118. *J. Comput. Chem.* **2003**, *24*, 1142−1156.

(114) Te Velde, Gt.; Bickelhaupt, F. M.; Baerends, E. J.; Fonseca Guerra, C.; van Gisbergen, S. J.; Snijders, J. G.; Ziegler, T. Chemistry with ADF. *J. Comput. Chem.* **2001**, *22*, 931−967.

(115) Hirata, S.; Head-Gordon, M. Time-dependent density functional theory within the Tamm-Dancoff approximation. *Chem. Phys. Lett.* **1999**, *314*, 291−299.

(116) Martin, R. L. Natural transition orbitals. *J. Chem. Phys.* **2003**, *118*, 4775−4777.

(117) Barker, T. J.; Denning, R. G.; Thorne, J. R. Applications of two-photon spectroscopy to inorganic compounds. 2. Spectrum and electronic structure of cesium uranyl nitrate, CsUO2 (NO3) 3. *Inorg. Chem.* **1992**, *31*, 1344−1353.

(118) Campbell, J.; Papp, T. Widths of the atomic K-N7 levels. *At. Data Nucl. Data Tables* **2001**, *77*, 1−56.

(119) Krause, M.; Oliver, J. Naturcal Wiciths of Atomic K and L Levels, Kor X-Ray Lines and Several Kii. Auger Lines. *J. Phys. Chem. Ref. Data* **1979**, *8*, 329.

(120) Reisler, H.; Krylov, A. I. Interacting Rydberg and valence states in radicals and molecules: experimental and theoretical studies. *Int. Rev. Phys. Chem.* **2009**, *28*, 267−308.

(121) Frati, F.; Hunault, M. O. J. Y.; de Groot, F. M. F. Oxygen K-edge X-ray Absorption Spectra. *Chem. Rev.* **2020**, *120*, 4056−4110.

(122) Kaufmann, K.; Baumeister, W.; Jungen, M. Universal Gaussian basis sets for an optimum representation of Rydberg and continuum wavefunctions. *J. Phys. B: At., Mol. Opt. Phys.* **1989**, *22*, 2223−2240.

(123) Southworth, S. H.; Dunford, R.; Ray, D.; Kanter, E.; Doumy, G.; March, A.; Ho, P.; Krässig, B.; Gao, Y.; Lehmann, C.; et al. Observing pre-edge K-shell resonances in Kr, Xe, and XeF 2. *Phys. Rev. A* **2019**, *100*, No. 022507.

(124) Knecht, S.; Repisky, M.; Jensen, H. J. A.; Saue, T. Exact two-component Hamiltonians for relativistic quantum chemistry: Two-electron picture-change corrections made simple. *J. Chem. Phys.* **2022**, *157*, No. 114106.

(125) Frati, F.; Hunault, M. O.; De Groot, F. M. Oxygen K-edge X-ray absorption spectra. *Chem. Rev.* **2020**, *120*, 4056−4110.

(126) Ogasawara, H.; Kotani, A.; Thole, B. T. Calculation of magnetic x-ray dichroism in 4d and 5d absorption spectra of actinides. *Phys. Rev. B: Condens. Matter Mater. Phys.* **1991**, *44*, 2169.

(127) van der Laan, G.; Figueroa, A. I. X-ray magnetic circular dichroismA versatile tool to study magnetism. *Coord. Chem. Rev.* **2014**, *277−278*, 95−129.

(128) Amidani, L.; Retegan, M.; Volkova, A.; Popa, K.; Martin, P. M.; Kvashnina, K. O. Probing the Local Coordination of Hexavalent Uranium and the Splitting of 5f Orbitals Induced by Chemical Bonding. *Inorg. Chem.* **2021**, *60*, 16286−16293.

(129) Bunău, O.; Ramos, A. Y.; Joly, Y. *International Tables for Crystallography*; International Union of Crystallography, 2021.

(130) Joly, Y.; Ramos, A. Y.; Bunău, O. *International Tables for Crystallography*; International Union of Crystallography, 2022.

(131) Tecmer, P.; Gomes, A. S. P.; Ekström, U.; Visscher, L. Electronic spectroscopy of UO_2^{2+}, NUO^+ and NUN: an evaluation of time-dependent density functional theory for actinides. *Phys. Chem. Chem. Phys.* **2011**, *13*, 6249.

(132) Tecmer, P.; Gomes, A. S. P.; Knecht, S.; Visscher, L. Communication: Relativistic Fock-space coupled cluster study of small building blocks of larger uranium complexes. *J. Chem. Phys.* **2014**, *141*, No. 041107.

(133) Oher, H.; Gomes, A. S. P.; Wilson, R. E.; Schnaars, D. D.; Vallet, V. How Does Bending the Uranyl Unit Influence Its Spectroscopy and Luminescence? *Inorg. Chem.* **2023**, *62*, 9273.

(134) Gomes, A. S. P.; Jacob, C. R.; Visscher, L. Calculation of local excitations in large systems by embedding wave-function theory in density-functional theory. *Phys. Chem. Chem. Phys.* **2008**, *10*, 5353.

(135) Bouchafra, Y.; Shee, A.; Réal, F.; Vallet, V.; Gomes, A. S. P. Predictive Simulations of Ionization Energies of Solvated Halide Ions with Relativistic Embedded Equation of Motion Coupled Cluster Theory. *Phys. Rev. Lett.* **2018**, *121*, No. 266001.

(136) Opoku, R. A.; Toubin, C.; Gomes, A. S. P. Simulating core electron binding energies of halogenated species adsorbed on ice surfaces and in solution via relativistic quantum embedding calculations. *Phys. Chem. Chem. Phys.* **2022**, *24*, 14390−14407.

https://doi.org/10.1021/acs.inorgchem.3c01302